PHYSICAL REVIEW B VOLUME 22, NUMBER 12 15 DECEMBER 1980

Ballistic phonon imaging in germanium

G. A. Northrop and J. P. Wolfe

Physics Department and Materials Research Laboratory, University of Illinois at Urbana-Champaign, Urbana, Illinois 61801

(Received 23 July 1980)

The anisotropic propagation of acoustic phonons in a single crystal of Ge at low temperatures is examined both experimentally and theoretically. We have devised a general heat-pulse imaging method which reveals the angular distribution of energy flux emitted from an incoherent point source of ballistic phonons. The resulting images contain remarkably complex two-dimensional variations in the phonon flux. The larger features of the flux patterns agree with previous numerical calculations of phonon focusing. Using only continuum elasticity theory and the known elastic constants for Ge, we find that the sharp features in the ballistic phonon image are explained by mathematical infinites in the phonon flux. Useful physical insights into the origin of these flux patterns are gained by graphically plotting (a) the locus of singularities on the constant-frequency $\vec{k}$-space surfaces and (b) the corresponding group-velocity surfaces. For a cubic crystal only two parameters (the ratio of elastic constants $C_{11}:C_{12}:C_{44}$) completely determine the flux pattern.

I. INTRODUCTION

The propagation of long-wavelength phonons in a crystalline solid is characterized by anisotropic velocities due to the direction-dependent elasticity of the medium. Measurements of sound velocities along several crystal directions are used to determine the elastic constants of a crystal accurately, as given by the fourth-rank elasticity tensor c_{ijlm}. Velocities of elastic waves can be determined to better than $10^{-2}\%$ accuracy using radio-frequency pulse-echo techniques. Even in a highly symmetric cubic crystal such as Ge, anisotropy in the sound velocity is significant (~30%). On the other hand, the thermal conductivity of a crystal is usually represented by a second-rank tensor, which for a crystal of cubic symmetry implies isotropic propagation of heat. The apparent discrepancy arises because the theory of thermal conductivity involves *diffusion* of high-energy acoustic phonons with mean free paths much shorter than the crystal length.

However, if one introduces a localized pulse of high-energy acoustic phonons (a heat pulse) into an otherwise cold crystal, such phonons may travel ballistically over macroscopic distances, displaying anisotropies directly associated with the elastic tensor. Unlike the coherent plane waves produced at rf frequencies by a quartz transducer, a heat pulse consists of incoherently generated phonons with roughly a Planck energy distribution characterized by the heater temperature.[1] For a typical heat pulse with $T = 10$ K, the maximum in the Planck distribution occurs at a frequency $\nu = 2.8k_BT/h \simeq 600$ GHz. Still, for Ge this is over an order of magnitude smaller than the Debye frequency, justifying the long-wavelength assumption. The heat-pulse method, originally demonstrated in crystals by R. J. von Gutfeld and A. H. Nethercot,[2] generally utilizes a resistive film to produce the heat pulse and a fast superconducting bolometer to detect the slight temperature rise when the ballistic phonons arrive at the opposite face of the crystal. The time-of-flight of these phonons across a crystal of known dimension is well explained by the sound velocities determined by rf means.

Shortly after these initial experiments it was observed that, in addition to the sound velocity, the phonon *energy flux* is dependent on the propagation direction. Taylor, Maris, and Elbaum[3,4] explained this "phonon-focusing" effect as a consequence of the noncollinearity of phase and group velocities. They presented statistical calculations of the angular-dependent flux enhancement which roughly explained their data. More detailed calculations by Rösch and Weis[5] and later by others[6] have predicted the heat flux emanating from a point source for a number of crystals with various symmetries.

The basic physics of phonon focusing is illustrated in Fig. 1 (Ref. 7). For an elastically anisotropic medium, a constant-frequency surface in $\vec{k}$ space is nonspherical, implying an anisotropic phase velocity, ω/k. This $\vec{k}$-space surface is also called the "slowness surface." Figure 1(a) is an actual slice of the constant $\omega(\vec{k})$ surface in the (001) plane for germanium, as calculated for a slow TA (STA) phonon mode in the next section. For a given wave vector $\vec{k}$ terminating on this surface, the energy flux is parallel to the group velocity, $\vec{V} = \partial\omega(\vec{k})/\partial\vec{k}$, which is normal to the surface. Thus, an isotropic distribution of $\vec{k}$ vectors, such as that emanating from an ideal point heat source, transforms into a distinctly anisotropic distribution of group ve-

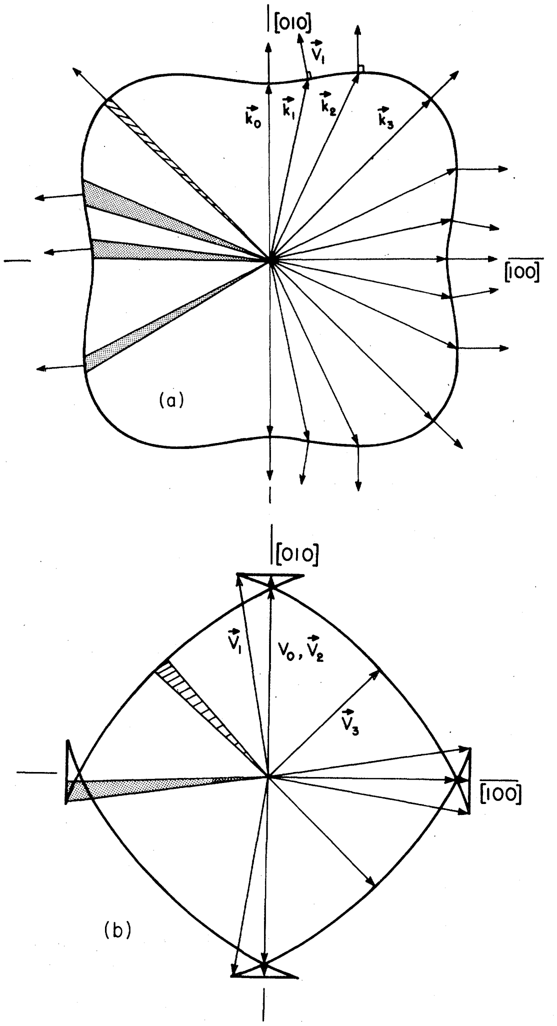

FIG. 1. (a) Intersection of a constant-frequency surface with the (001) plane for the slow TA mode in Ge. The shape of this surface, also known as the slowness surface, is independent of ω for linear dispersion $\omega = v(\theta_k, \phi_k)k$, appropriate to the long-wavelength limit. The group velocities are normal to the surface and in general are not collinear with $\vec{k}$. (b) Plot of the group velocities corresponding to the $\vec{k}$ vectors in (a). The resulting group-velocity surface contains folds, e.g., at $\vec{V}_1$. Two equal "solid-angle" sections along different $\vec{V}$ directions are shown in the left side of the diagram. A mapping of these two real-space sections into $\vec{k}$ space is shown in the left half of Fig. 1(a). The upper $\Delta\Omega_V$ maps into a single smaller $\Delta\Omega_k$, implying a "defocusing" of phonon flux ($A < 1$). The $\Delta\Omega_V$ which crosses three branches of the $\vec{V}$ surface maps into three different $\vec{k}$ directions and the flux enhancement along this group-velocity direction is large.

locities, as illustrated in the figure. Phonon energy is concentrated, or "focused," along $\vec{V}$ directions for which the curvature of the constant-frequency surface is small.

The calculations of Maris[8] and of Rösch and Weis[5] consisted of determining the ratio of the $\vec{k}$-space solid angle $\Delta\Omega_k$ to the corresponding $\vec{V}$-space solid angle $\Delta\Omega_V$ for a finite grid of real-space ($\vec{V}$-space) directions. That is, assuming an isotropic distribution of $\vec{k}$ vectors, they determined the angular density of corresponding $\vec{V}$ vectors. The enhancement factor, $A \equiv |\Delta\Omega_k/\Delta\Omega_V|$ is proportional to the phonon energy flux and is equal to unity for an isotropic medium. The physical idea is contained in the left half of Figs. 1(a) and 1(b). Figure 1(b) is a plot of the slow TA group velocities in the (001) plane of Ge. A constant real-space solid angle $\Delta\Omega_V$ subtended by a detector corresponds to one or more $\vec{k}$-space solid angles $\Delta\Omega_k$, differing in magnitude and location. Phonon energy emanating from a heated *point source* in the crystal is concentrated along directions where A is large. These high-intensity directions are not in general along crystal symmetry axes, but are determined by the ratios of elastic constants.

The theoretical results of Rösch and Weis displayed remarkably complex phonon focusing patterns for all crystals considered, with immense variation in phonon intensity within a given phonon mode. Indeed, as these authors noted, there are directions along which the enhancement factor is mathematically infinite (yet integrable), even for crystals with a nearly isotropic elastic tensor (e.g., sapphire). An example of a point where A diverges in Ge is labeled by the vector $\vec{k}_1$ in Fig. 1. At this point there is an inflection in the curvature of the constant-ω surface.

Sharp features in the phonon flux in Ge were experimentally observed by Hensel and Dynes,[9] who were using heat pulses to study the absorption of phonons by electron-hole droplets. They introduced the heat pulse at the crystal surface via a pulsed laser. By rotating their crystal about a symmetry direction, they were able to continuously vary the propagation direction to the detector. In later papers[10,11] they reported comparisons of their one-dimensional scans with results calculated from a modified version of Maris' computer program. They found a good semiquantitative agreement.

In this paper we describe in detail a general new experimental method which provides a new approach to the phenomenon of phonon focusing. The method, which we call ballistic phonon imaging, produces a two-dimensional map of the phonon intensities emanating from a point source in the crystal. One result is a precise map of the phonon flux singularities. The resulting photographs contain details of the intensity structures which exceed those in previous calculations. Figure

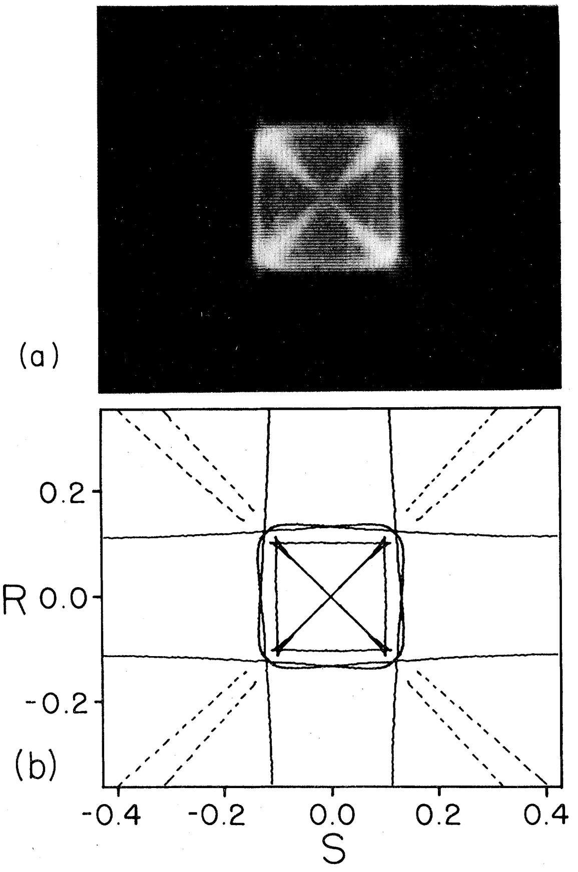

FIG. 2. (a) Ballistic phonon image for Ge. Bright regions indicate high phonon flux impinging on the (001) face of the crystal. This image represents a scan of 48° in propagation direction from left to right, with the [001] direction at the center of the pattern. The reader may find it useful to imagine a point source of phonons at the center of the pattern on the opposing face of the crystal (Ref. 14). (b) Calculated lines of mathematically infinite phonon flux for the xy scan in the image above. The solid lines are for the slow TA phonons and dashed lines are for fast TA phonons. The FTA singularity lines actually continue to the center. The axes are related to the propagation angles (θ_V, ϕ_V) by the relations $R=-\tan\theta_V \sin(\phi_V - \pi/4)$ and $S=\tan\theta_V \cos(\phi_V - \pi/4)$ obtained from Fig. 4(a).

2(a) shows the first experimental determination of the phonon focusing pattern in a crystal.[12,13] The larger features of this data verify the theoretical predictions of Rösch and Weis.[5] Bright regions are points of high phonon flux arriving at a $\{100\}$ face of a Ge crystal. In effect,[14] the phonon source is at the center of this pattern on the opposite face.

To explain the origin of these complex intensity patterns we have devised a somewhat different approach to the theoretical problem, which lends some further physical insights into the source of the singularities. We calculate the complete locus of points on the slowness surface for which the enhancement factor A diverges. These singularities are lines which separate regions of positive and negative Gaussian curvature of the slowness surface. The link between these singularity lines and the real-space flux patterns is made by plotting the actual group-velocity surfaces. The locus of all points $\vec{V}$ from the origin define a group-velocity surface which is much more complex than the slowness surface, as is simply illustrated in Fig. 1(b). The group-velocity surfaces contain folds[15] (e.g., at $\vec{V}_1$) which correspond to zero curvature of the slowness surface (e.g., at $\vec{k}_1$). These folds define the real-space directions of the singularities and are found to form boundaries between strong and weak focusing directions. Figure 2(b) shows the expected singularities in phonon flux for the experimental geometry, as explained in Sec. V.

One advantage of this approach is that the anisotropic propagation of the phonons is characterized by a pattern of well defined and measurable structure. Indeed, the structure of this pattern contains all of the necessary information to determine the ratios of elastic constants. The experimental method also gives a detailed map of the relative phonon intensities. However, the calculation of A as a function of propagation angle meets with several difficulties. The enhancement A is an analytic function in $\vec{k}$, but $\vec{k}$ is not readily obtainable for a given $\vec{V}$; indeed, there may be several different $\vec{k}$ directions producing the same $\vec{V}$ direction. Contributions from all such branches must be added to obtain a total enhancement. Furthermore, for comparison with experiment, A must be integrated over the detector area; thus, peak intensities (especially near infinities in A) will depend on detector shape and size.[16] Finally, neither the actual angular $\vec{k}$-space distribution of phonons nor the angular dependence of their attenuation are known. Ultimately, comparison of the experimental intensities with theory may determine these factors. However, none of these factors directly affect the geometrical focusing pattern.

In the past, heat-pulse experiments have been used to investigate many phenomena, such as the onset of diffusive propagation,[17] scattering at boundaries, Kapitza resistance, scattering due to impurities,[18-20] and phonon absorption by electron-hole liquid.[21] Most of this work exploited temporal analysis of heat-pulse intensity. The quantitative imaging method demonstrated in our experiment is a powerful extension of this technique and should provide a general tool for investigation in such areas.

Two other experimental efforts directly concerned with the phonon focusing patterns in crystals have appeared concurrently with our work. Eisenmenger[22] has produced remarkable two-dimensional patterns of the phonon focusing effect in Ge and Si using the fountain effect of superfluid He. Taborek and Goodstein[23-25] have calculated the theoretical phonon flux singularities for sapphire, discussed the application of catastrophe theory to singularities, and uncovered effects of phonon focusing on crystal–liquid-He boundary reflections.

II. THEORY OF PHONON FOCUSING

The phenomenon of phonon focusing is based on classical elasticity theory, assuming wavelengths long enough to ignore dispersion ($\lambda \gg a_0$, with a_0 the lattice constant). The medium is modeled as continuous but anisotropic. The problem of elastic wave propagation in an anistropic medium has been treated in detail by a number of workers,[26] with recent treatises given by Musgrave[27] and by Federov.[28]

The propagation equation for elastic waves in a solid begins with a generalized statement of Hookes Law. The stress σ_{ij} is related to the strain e_{lm} by the linear relation

$$\sigma_{ij} = c_{ijlm} e_{lm} , \tag{1}$$

with c_{ijlm} the elastic tensor of the solid. For a crystal of cubic symmetry, just three independent parameters define the nonzero elements of the elastic tensor: $c_{iiii} \equiv C_{11}$, $c_{iijj} \equiv C_{12}$, and $c_{ijij} \equiv C_{44}$, with $i \neq j$ and subscripts denoting axes along the edges of the cube. At a position vector $\vec{x} = (x_1, x_2, x_3) = (x, y, z)$ in the solid, a displacement of the atoms from their equilibrium position is denoted by $\vec{u}(\vec{x}) \equiv (u_x, u_y, u_z)$. The strain associated with this displacement is defined by $e_{lm} = \partial u_l / \partial x_m$.

The acceleration $\ddot{\vec{u}}$ of a small-volume element is proportional to the stress gradient, and for a crystal of density ρ the wave equation is given by

$$\rho \ddot{u}_i = \frac{\partial \sigma_{il}}{\partial x_j} = c_{ijlm} \frac{\partial^2 u_l}{\partial x_j \partial x_m} . \tag{2}$$

In this paper, summation is assumed over repeated indices. The plane-wave solution for displacement is $\vec{u} = \vec{\epsilon} e^{i(\vec{k} \cdot \vec{x} - \omega t)}$, where $\vec{\epsilon}$ is the polarization vector, $\vec{k}$ is the wave vector, and ω is the angular frequency of the wave. Substitution of this solution into Eq. (2) yields an eigenvalue equation:

$$(c_{ijlm} k_j k_m - \rho \omega^2 \delta_{il}) \epsilon_l = 0 . \tag{3}$$

Defining the wave normal $\vec{n} = \vec{k} / |\vec{k}|$ and the phase velocity $v = \omega / |\vec{k}|$ and dividing by $\rho |k|^2$, Eq. (3) becomes

$$(D_{il} - v^2 \delta_{il}) \epsilon_l = 0 , \tag{4}$$

with $D_{il} = (1/\rho) c_{ijlm} n_j n_m$ the Christoffel tensor.[29] The nondispersive nature of this formulation is now clear. Since D_{il} depends only on the direction of $\vec{k}$, the phase velocity v for a given direction $\vec{n}$ is independent of $|\vec{k}|$. For a given wave-vector direction, $\vec{k} = (k, \theta_k, \phi_k)$, the frequency of the wave is

$$\omega = v(\theta_k, \phi_k) k . \tag{5}$$

The phase velocity $v(\theta_k, \phi_k)$ can be obtained by solving the characteristic equation of (4):

$$\det(D_{il} - v^2 \delta_{il}) = 0 . \tag{6}$$

This is a cubic equation in v^2, with three roots corresponding to a longitudinal and two transverse phonon modes. For each root, v_α, there is a polarization vector $\vec{\epsilon}_\alpha$, where $\alpha \equiv 0, 1, 2$. For a given $\vec{k}$ vector, the three polarization vectors $\vec{\epsilon}_\alpha$ will be mutually orthogonal; however, in general none will be parallel or normal to $\vec{k}$. We identify $\alpha = 0$ with the predominantly longitudinal mode (LA) and $\alpha = 1, 2$ with the slow (STA) and fast (FTA) transverse modes, respectively.

The energy flux for an elastic wave is parallel to the group velocity. By vector differentiation of Eq. (5), we obtain

$$\mathrm{V} = \frac{\partial \omega}{\partial \vec{k}} = \left(v - \vec{n} \cdot \frac{\partial v}{\partial \vec{n}} \right) \vec{n} + \frac{\partial v}{\partial \vec{n}} . \tag{7}$$

We have found that the derivative $\partial v / \partial \vec{n}$ is obtained most simply by implicit differentiation of Eq. (6), as described in the Appendix.

The direction of energy flux (θ_V, ϕ_V) is obtained from the group-velocity components, which in turn depend on (θ_k, ϕ_k). This $\vec{k}$-space to $\vec{V}$-space transformation may be expressed as

$$\begin{aligned} \cos\theta_V &= f(\cos\theta_k, \phi_k) \\ \phi_V &= g(\cos\theta_k, \phi_k) , \end{aligned} \tag{8}$$

where the functions f and g are determined from the components of $\vec{V}$ above. Equations (8) are a mapping of one two-dimensional space (θ_k, ϕ_k) into another two-dimensional space (θ_V, ϕ_V). The ratio of the product of differentials in these two spaces is the Jacobian of the functions f and g:

$$d\Omega_V = d(\cos\theta_V) d\phi_V = J d(\cos\theta_k) d\phi_k = J d\Omega_k , \tag{9}$$

with

$$J \equiv \det \begin{bmatrix} \dfrac{\partial f}{\partial \cos\theta_k} & \dfrac{\partial f}{\partial \phi_k} \\ \dfrac{\partial g}{\partial \cos\theta_k} & \dfrac{\partial g}{\partial \phi_k} \end{bmatrix} . \tag{10}$$

This last result provides the desired link between the mathematical formalism and the phonon intensities. The enhancement factor A is simply related to the Jacobian by

$$A \equiv \left| \frac{\Delta\Omega_k}{\Delta\Omega_V} \right| = \frac{1}{|J|}. \tag{11}$$

The geometrical interpretation of the Jacobian J is that $J = K|k|^2\cos\zeta$, where K is the Gaussian curvature of the slowness surface and ζ is the angle between $\vec{k}$ and $\vec{V}$. The Gaussian or total curvature is the product of the two extremal curvatures (inverse radii) of an elemental surface. If either or both of the extremal curvatures vanish, J and K will vanish. Of course, J as defined in Eqs. (8)–(10) is more fundamental to our present studies than K. The Jacobian is dimensionless and directly related to the physical enhancement factor A by Eq. (11).

In principle the problem is now solved. One can calculate this enhancement at all angles for comparison to experiment. This is accomplished by a computer program which, given the density ρ, the elastic constants c_{ijlm}, the $\vec{k}$-vector direction (θ_k, ϕ_k), and the mode index α, calculates v, $|\vec{V}|$, θ_V, ϕ_V, and J. This program is used to create the $\vec{k}$- and $\vec{V}$-space surfaces of Sec. V, and will be published separately. The primary difficulty in obtaining the real-space enhancement is that J, as expressed in Eq. (10), is a function of (θ_k, ϕ_k), whereas energy propagation is observed along the corresponding (θ_V, ϕ_V). This requires inverting the mapping of Eq. (8), which must be done point-by-point. In fact this inverse mapping is generally not unique; there are cases where one (θ_V, ϕ_V) results from several different (θ_k, ϕ_k), as illustrated in Fig. 1.

We have discovered that a calculation of the directions (θ_k, ϕ_k) where $J = 0$, corresponding to mathematically infinite enhancement, provides both a useful insight into the physics and a quantitative means of analyzing the ballistic phonon patterns. The condition $J = 0$ defines a locus of points on the slowness surface which separate regions of positive and negative Gaussian curvature. This will be discussed in detail for Ge in Sec. V. Once these singularity lines are determined by a simple root-finding routine, the associated real-space directions (θ_V, ϕ_V) for intense focusing can be found. As we will see for the TA modes in Ge, the $J = 0$ patterns explain all the detailed structure in the ballistic phonon image.

III. EXPERIMENTAL METHODS

The heat-pulse method has been described in detail in an early review article by von Gutfeld.[30] Typically, a heat pulse is produced by passing a short (0.1–1 μs) pulse of current through a resistive heater (e.g., a constantan film) evaporated onto the crystal surface. This heater radiates phonons with roughly a Planck energy distribution. At low temperatures these phonons traverse the sample ballistically and are detected as a small temperature rise in a bolometer. The bolometer consists of a strip of superconductor evaporated onto the crystal face opposite the heater. The crystal is cooled to the transition temperature of this superconducting bolometer. Depending on film thickness and material, a transition from near zero to about 100 Ω resistance occurs over a small temperature range, providing a sensitive detector of minute temperature changes. Since the thermal heat capacity of this film is very small, the bolometer is capable of sensing heat pulses with a time resolution of 10–100 ns.

The present experiments differ from previous approaches in several respects. First, in order to achieve high solid-angle resolution, it was necessary to fabricate a bolometer with very small dimensions. Figure 3 shows the structure of a 220×180 μm^2 granular-aluminum bolometer and its resistance in the superconducting transition region. A mask consisting of a slit and six microscopically positioned copper wires (diameter 12 μm) produced this pattern. The thickness of the film was typically 300 Å. For optimal sensitivity and linearity an operating temperature near the maximum slope in $R(T)$ was chosen. The temperature was accurately controlled by regulating the vapor pressure of the ^{4}He bath in which the sample was immersed. For a

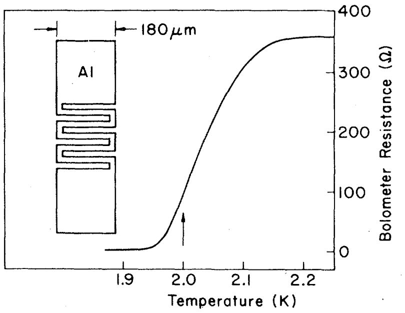

FIG. 3. Measured electrical resistance of an Al thin-film bolometer as the temperature is lowered through the superconducting transition. In a heat-pulse experiment, the temperature of the crystal and bolometer is biased at a point where dR/dT is a maximum, as indicated by the arrow, by regulating the pressure of the helium bath. Inset: Diagram of the Al film geometry which produces a bolometer with very small sensitive area and hence high solid-angle resolution.

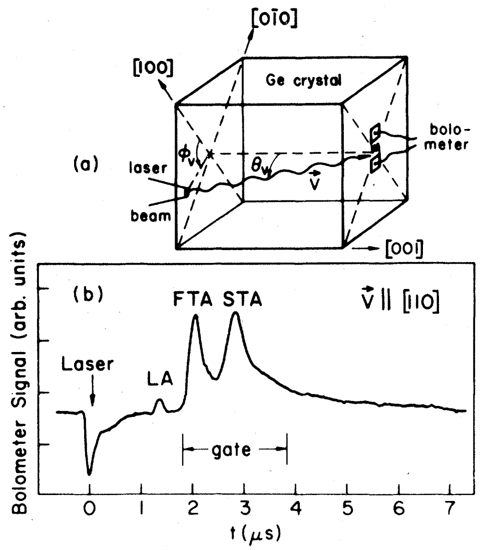

FIG. 4. Schematic of the experiment showing a laser-produced heat pulse and bolometer geometry for detection of ballistic phonons. Angles (θ_V, ϕ_V) define the propagation direction of the phonon flux striking the detector. (b) Bolometer signal showing the arrival of various phonons for the [110] propagation direction. A typical boxcar gate for the imaging experiment is shown.

typical crystal with 1 cm^3 dimensions, the bolometer subtended about 1° angular resolution from a point source on the opposite face.

Second, the heat pulse, produced by pulsed laser beam, was accurately and automatically scanned in two dimensions across the surface of the crystal. The technique of *xy* scanning the heat source with respect to a single fixed detector is equivalent to having a large array of identical detectors. The laser was a *Q*-switched Nd:YAIG ($\lambda = 1.06$ μm) with a typical peak power of 10 W and pulse width of 200 ns. The *xy* scanning was accomplished by rotation of two deflection mirrors via precision galvanometers.[31] The beam was focused to a 100-μm spot size on the crystal surface. Similar heat-pulse signals were obtained whether the excitation surface was metallized or not. The absorption length of 1.06-μm-wavelength light in Ge is about 1 μm and acoustic phonons are generated as a product of the rapid thermalization of photoexcited carriers.

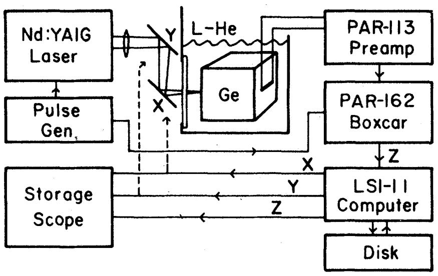

FIG. 5. Schematic diagram of the experimental apparatus in the heat-pulse imaging experiment. The LSI-11 computer controls the raster scanning of the pulsed laser beam via a two-axis mirror deflection system. The laser is typically pulsed (via a *Q* switch) at a repetition rate of 2 kHz. The time-resolved output from the boxcar averager is accumulated by the computer in a 256 × 256 array. This array of phonon intensities may be stored in the disk or displayed on a storage oscilloscope.

Figure 4(a) is a drawing of the heat-pulse experiment showing the crystal symmetry axes pertinent to Fig. 2 and defining the propagation direction of the detected phonons. A signal-averaged trace of the ballistic phonon signals arriving at the detector for one particular (θ_V, ϕ_V) is shown in Fig. 4(b). The negative-going pulse at $t = 0$ marks the time of the laser pulse and is due to a photocurrent shunting the bolometer. The arrival time of the three phonon modes depends on their respective group velocities. A boxcar averager may be used to sample the signal at various times after the laser pulse. The boxcar produces an output voltage proportional to the integrated signal within a preset time window or gate. The time gate shown in Fig. 4(b) results in an output voltage proportional to the sum of the integrated TA phonon intensities, but one insensitive to the LA signal. As the laser beam is translated across the crystal face, the arrival times of the phonons will vary by approximately 30%. In the experiment of Fig. 2 the broad gate in Fig. 4(b) was chosen to sample the time-integrated TA phonon signal for a wide range of propagation directions (±24° left to right from the center). A storage oscilloscope is raster scanned synchronously with the laser beam, and the intensity of the cathode-ray tube (CRT) is modulated by the boxcar output, which produces bright regions where there are intense phonon signals. Figure 2 is a photograph of the oscilloscope face.

Because of the immense amount of information contained in a single image, an LSI-11 microcomputer system is employed to digitally store the phonon intensities in a 256 × 256 element array. In fact, the computer is also used to accurately control the raster scanning of the laser beam. This is accomplished by deflecting the galvanometer-driven mirrors with digital-to-analog converters. An overall schematic of the experimental arrangement is shown in Fig. 5. In the initial setup and alignment, a complete image is recorded in real time on the storage oscilloscope in about a minute using 20 Hz horizontal and 0.01 Hz vertical scanning rates.

The computer plays a central role in both the

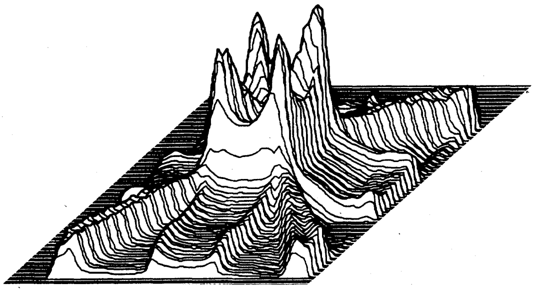

FIG. 6. Pseudo-3D hidden-line representation of the image in Fig. 2(a). The four peaks near the center represent the corners of the outer square. Both the STA ramps and the FTA ridges are apparent.

acquisition and the analysis of the data. It permits signal averaging of the ballistic phonon image over an extended period of time. The image in Fig. 2 was an average over 10 min; however, a complete image could be recorded in less than a minute with some sacrifice in the signal-to-noise ratio. The image is stored on a floppy-disk medium with 12-bit intensity resolution, permitting 8 images to be stored on a single disk. The digitally stored data contains a remarkable amount of quantitative information which can be easily accessed and analyzed with the computer. One useful application, shown in Fig. 6, is a hidden-line pseudo-three-dimensional representation of the image in Fig. 2, showing the relative TA phonon intensities in Ge on a linear scale.

In order to obtain a high-resolution mapping of the intricate TA phonon focusing pattern about the [001] axis, a longer sample of Ge with dimensions $1.5\times1.5\times2.7$ cm^3 was employed. This sample was cut with all {100} faces from a crystal[32] of ultrapure Ge and afforded a threefold increase in temporal and spatial resolution. With the bolometer dimensions stated above, the angular resolution was 0.4° of arc. The resulting images, shown in the next section, allowed a more detailed comparison with the theory.

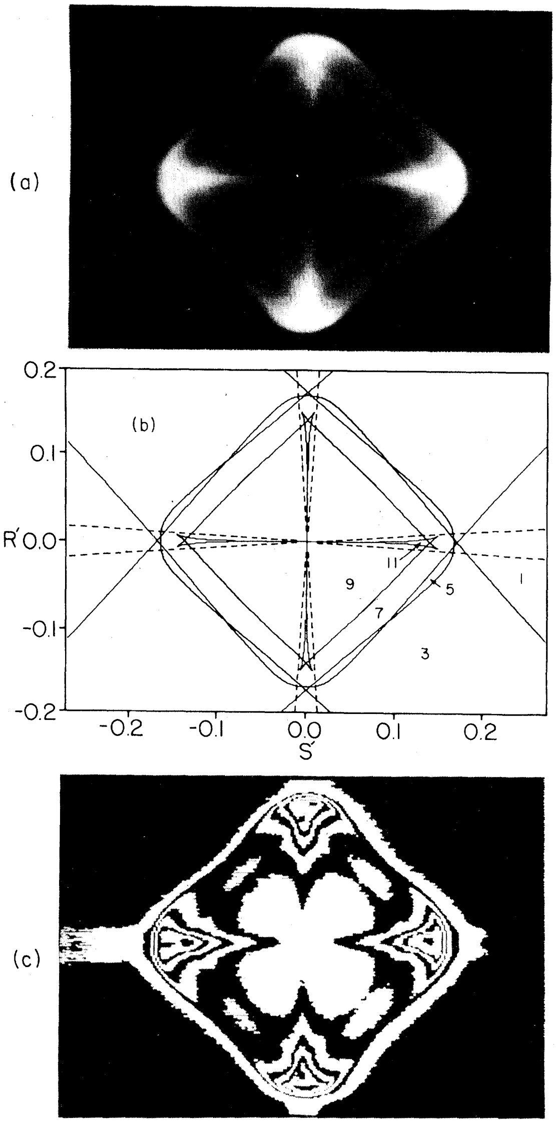

FIG. 7. (a) Magnified view of the TA phonon focusing structure near the [001] axis. The improved angular resolution and detail in the image results from the longer phonon path length in this crystal. The inner square and associated detailed structure is clearly visible in this photograph. (b) Calculated $J=0$ lines for the same range of propagation directions as the above image. Solid lines are STA and dashed lines are FTA phonons. The integers indicate the number of branches of the group-velocity surface for the STA mode. The axes are related to the propagation angles (θ_V, ϕ_V) by the relations $R' = -\tan\theta_V \sin\phi_V$ and $S' = \tan\theta_V \cos\phi_V$ from Fig. 4(a). (c) Contour map of the ballistic phonon image in (a) defining curves of constant intensity.

IV. EXPERIMENTAL RESULTS

The ballistic phonon image shown in Fig. 2(a) and quantitatively represented in Fig. 6 contains the major features of phonon focusing for the TA phonon modes in germanium. All of the local maxima in intensity correspond to integrable $J=0$ singularities in the phonon flux, as seen from Fig. 2(b). The measured peak height, of course, depends upon the solid angle subtended by the detector. These local maxima define boundaries between higher and lower flux enhancement, giving rise to the STA "ramps" and FTA "ridges" radiating outward from the [001] symmetry axis. As we will see in Sec. V, each propagation direction within the ramps or ridges corresponds to three distinct $\vec{k}$-space directions, owing to folds in the velocity surface. The bright central square with sides $\pm7.5°$ from the [001] axis has its origin in the slow TA mode. A less intense inner square can also be discerned in the photograph. Depending upon the propagation angle, each group-velocity direction within the bright square may correspond to 5, 7, 9, or 11 distinct $\vec{k}$ vectors, partly accounting for the large enhancement in this region. We begin this section by describing experiments on the long (2.7-cm) crystal, which allowed a detailed look at the intricate structure near the [001] propagation direction.

A ballistic phonon image for this crystal is shown in Fig. 7(a). This photograph subtends a total of 30° of arc from left to right. The bright square is rotated 45° with respect to the image of Fig. 2(a), owing to the different crystal orientation. The theoretical $J=0$ pattern for this magnification is shown in Fig. 7(b), using the previously measured[33] elastic constants $C_{11}:C_{12}:C_{44}::1.0:0.38:0.52$. The bright regions in the experimental image are found to agree with the theory, within the resolution of the bolometer.

Once the image is recorded in digital form, the information can be probed and displayed in a variety of ways. The shape of the two-dimensional intensity surface is exposed by constructing a contour map of the digitally recorded image. Figure 7(c) displays constant intensity lines as borders between black and white regions. The black and white regions define equal intervals in phonon intensity; e.g., 10 to 20 is black, 20 to 30 is white, etc.

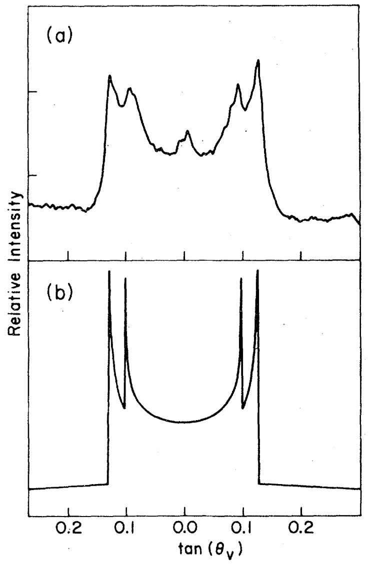

FIG. 8. (a) Scan of the phonon flux intensities in the (011) plane, obtained from a digitally stored image similar to Fig. 7(a). The small structure at the center arises from singularities in the (100) and (010) planes. These are detected due to the finite detector size. (b) Calculation of the enhancement factor $A=1/|J|$ for the same propagation directions as in (a).

Another comparison with theory, shown in Fig. 8(a), is a diagonal scan across the image, along the crystal [011] axis and through the center of the square.[34] Figure 8(b) is the calculated enhancement factor, $A=1/|J|$, for this scan. This involves an analytic calculation of $A(\theta_V,\phi_V)$, summed over all branches for each (θ_V,ϕ_V), without averaging over a finite detector solid angle. The peak heights of the singularities depend upon the sampling interval as the computer steps in propagation direction. The experimental position of the outer singularity at 7.5° from [001] agree well with the theoretical value 7.4° based on the above elastic constants. The inner box at 5.5° is discernibly smaller than the predicted singularities at 5.7°. This small discrepancy is less than the nominal bolometer resolution.

The time of flight for phonons to traverse the crystal is L/V, where $L=l\cos\theta_V$ is the phonon path length for a crystal of length l and $V=|\vec{V}(\theta_V,\phi_V)|$ is the magnitude of the group velocity. Actually, for a given mode α and propagation direction (θ_V,ϕ_V) there may be several values of V arising from different branches of the velocity surface. For the above crystal with $l=2.7$ cm, the TA phonon times of flights vary between 7 and 9 μsec; the LA phonon times of flights fall in the 5 to 6 μsec range. Since the width of the detected heat pulses is limited only by the relatively short laser pulse length (variable from 200 to 300 ns), it is possible to resolve various features of a ballistic phonon pattern by proper selection of the boxcar delay time and gate width. [See Fig. 4(a).] For propagation exactly along [001] both STA and FTA velocities are degenerate by symmetry. However, this degeneracy is lifted for finite (θ_V,ϕ_V) and with a sufficiently high-time resolution one can distinguish experimentally the FTA and STA components in the image by their differing times of flight.

An informative sequence of images has been obtained by using a relatively narrow (300-ns) gate width and a progression of delay times. The resulting images are represented in Fig. 9 as pseudo-three-dimensional graphs of the structure near [001]. This is the same view as in Fig. 7(a). As the detection gate is translated further in time from the laser pulse, one can see relative changes in (a) the four peaks at the corners of the outer square, (b) the sides of the outer square, (c) the intensity of the inner square, and (d) the STA ramps and FTA ridges outside the square region.

As previously noted, the square pattern comes

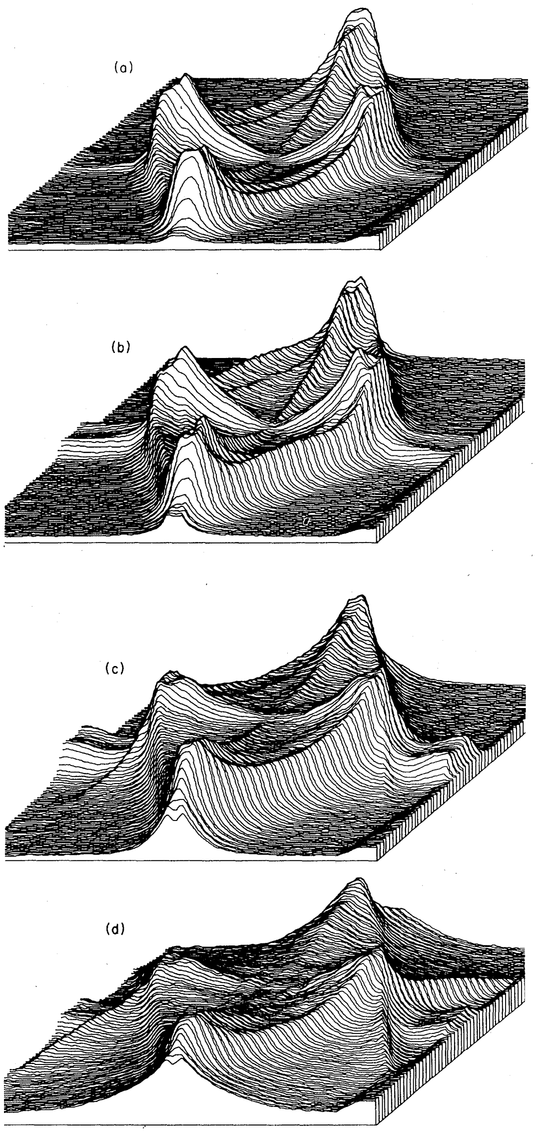

FIG. 9. Pseudo-3D representation of the phonon intensities as a function of delay time after the laser pulse. The scanning range is that of Fig. 7(a). Various features in the phonon flux enhancement pattern are emphasized as different group velocities are sampled. (a) 7.6-μs delay, 200-ns gate width; (b) 7.75-μs delay, 300-ns width; (c) 8.15-μs delay, 300-ns width; (d) 8.55-μs delay, 300-ns width.

from the STA mode. Yet the corners of the square are the first features to appear in time, even before the FTA ridges. This implies that the STA group velocities are actually larger in these directions than the FTA group velocities—a fact which is verified in the calculation of $\vec{V}$. One might reasonably question the use of the terms "fast" and "slow" at this point.[35] As we shall see in Sec. V, these terms more appropriately refer to the *phase* velocities of the elastic wave. Except for the degenerate symmetry points, the slowness surface for the FTA mode always lies inside the slowness surface of the STA mode.

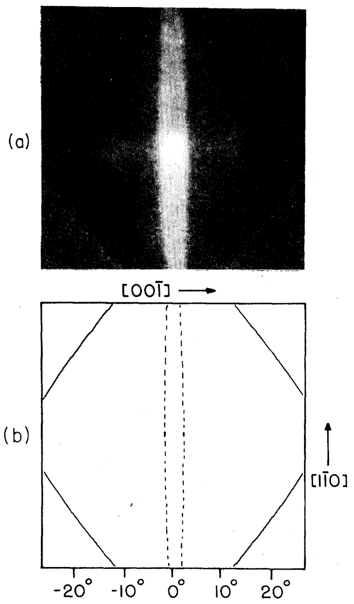

FIG. 10. (a) Phonon intensities obtained by scanning the heat pulse across a $(\bar{1}\bar{1}0)$ face and detecting with a bolometer at the center of the opposing (110) face. (b) Predicted $J = 0$ lines for the experimental geometry above. STA lines are solid and FTA lines are dashed. The scale at the bottom measures the propagation angle, in degrees, from the [110] axis.

At a slightly later time, Fig. 9(b), the FTA ridges begin to appear and the inner structure is most developed. In Fig. 9(c) the intensity of the square has filled in, and there is a simultaneous loss of fine structure. In the final image at a still later time, the STA ramps become prominent. This time sequence of the ballistic phonon pattern is in qualitative agreement with theoretical calculations of the group velocities of the TA phonons.

Up to this point we have discussed the ballistic phonon pattern within about 25° of the [001] propagation direction (Fig. 2). A more complete picture may be obtained by choosing several different excitation-detection geometries. The 1-cm^3 crystal shown in Fig. 4(a) has four $\{110\}$ faces and two $\{100\}$ faces. A different range of propagation directions is obtained by depositing a bolometer on the center of the (110) face and scanning the heat pulse across the opposing face. The result is shown in Fig. 10(a). The center of this pattern corresponds to the [110] propagation direction. The intense vertical strip is the FTA ridge. As indicated in Fig. 2 and predicted by the calcula-

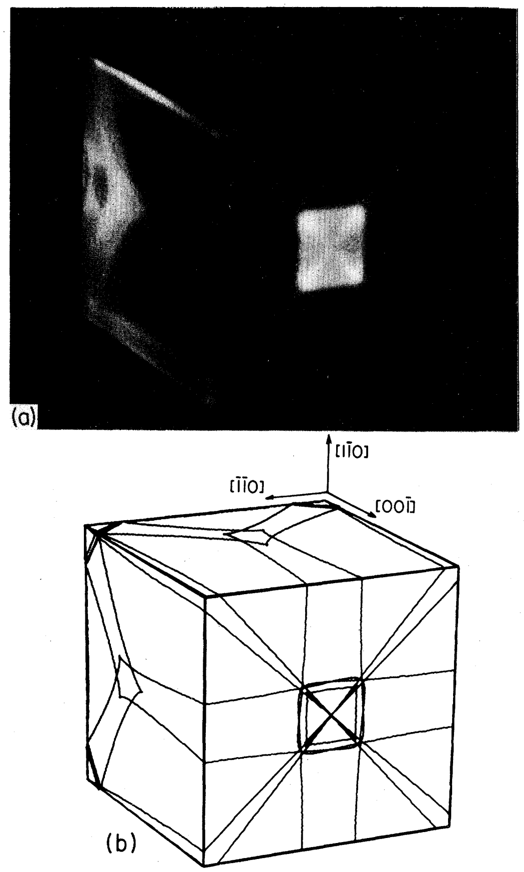

FIG. 11. (a) Ballistic phonon image with laser beam obliquely incident on three sample faces. The bolometer is in the center of the back left (001) face. (b) Calculated $J = 0$ singularities projected onto an equivalent cube.

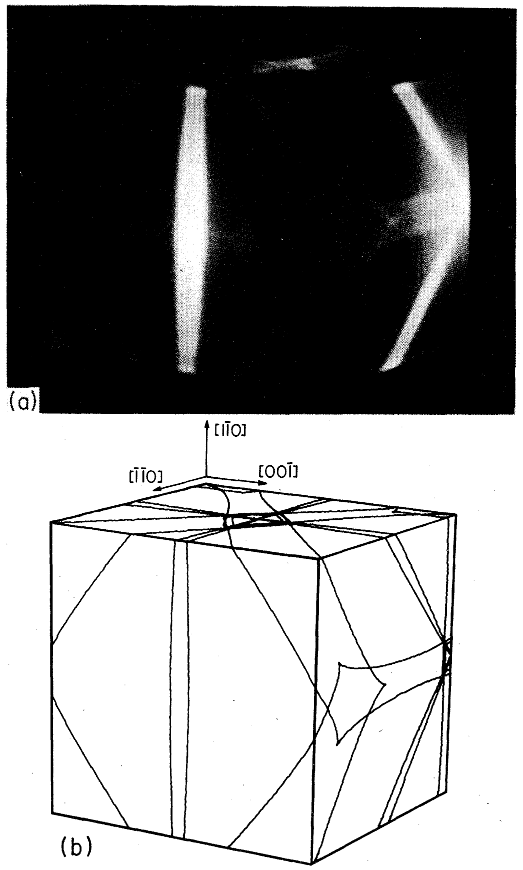

FIG. 12. (a) Same as 11(a) except slightly different orientation and with the bolometer in the center of the back right (110) face. (b) Calculated $J = 0$ singularities projected onto an equivalent cube.

tions of Rösch and Weis,[5] these ridges lie in the three $\{100\}$ planes of the crystal. The $J = 0$ singularities of the FTA mode are displaced between 0° at $\langle 100\rangle$ and 2° at $\langle 110\rangle$ from the $\{100\}$ planes, Also visible at the corners of this image are the STA ramps. The calculated $J = 0$ lines for this experimental geometry are plotted in Fig. 10(b), showing excellent agreement with theory.

Of course, there is no particular reason why the excitation beam must be normally incident to a crystal face as in the experiments above. To take advantage of this, we simply mounted the 1-cm^3 crystal at an oblique angle to the laser beam, so that a maximum number of crystal faces (three) could be excited within a single image. The result was a global picture of the phonon focusing effect in Ge. Using a wide time gate to encompass the greater variation in phonon path length, we obtained the photograph in Fig. 11(a). The bolometer was located at the center of the face farthest from the viewer; the (001) face. By scanning the laser beam over an area larger than the crystal, a striking "three-dimensional" view of the entire crystal resulted. A completely different picture is obtained by using the bolometer located on the center of the (110) face, as is shown in Fig. 12(a). The crystal was rotated slightly to better expose the $(\bar{1}\bar{1}0)$ face. In fact, both bolometers were operational during the same experimental run, and the two different patterns could be obtained by simply switching bolometer connections, without adjusting crystal orientation or laser scanning range. As in all of the ballistic phonon images, the reader may find it useful to view the fixed bolometer as the point source of phonons. The bright regions then correspond to high phonon intensities striking the other crystal faces.

A direct comparison of these images with theory is made by projecting the $J = 0$ singularities onto the appropriate crystal surfaces shown in Figs. 11(b) and 12(b). These computer plots are drawn in perspective. The data and theory clearly show the FTA ridges in the $\{100\}$ planes as well as the joining of the STA ramps near the $\langle 111\rangle$ axes. This three-cusp structure near ⟨111⟩, especially prominent in Fig. 12(a), will be discussed in detail in Sec. V.

The ballistic phonon imaging method will likely be useful in another important area—reflection of phonons from boundaries. For a crystal immersed in liquid helium, the transmission of phonons across the liquid-solid interface is known to be much higher than expected from simple acoustic mismatch theory. This anomalously low thermal boundary resistance, first observed by Kapitza, has been a topic of much interest and controversy.[19,20] Using the imaging method it is possible to make an absolute measurement of the reflection coefficient for phonons in a heat pulse. In Fig. 12(a) one can observe a sharp but dimmer structure not predicted by Fig. 12(b). These extra lines are due to phonons specularly reflected from other crystal faces. This reflection pattern may be somewhat enhanced by using longer boxcar delay times corresponding to the longer reflected path lengths. The specular reflection of $J=0$ singularities from the top surface of the cube onto the other surfaces is shown in Fig. 13. Many of these features can be detected in the image. By scanning across the image along the arrow marked S in Fig. 13, a comparison was made between the intensity of direct and reflected phonons. For this mode (STA) and propagation direction $(\theta_k, \phi_k; \theta_V, \phi_V) = (72.4,\ 29.0;\ 71.6,\ 10.3)$, we found a reflection coefficient $R = 0.20 \pm 0.08$. Using this method it should be possible to make a systematic study of R for various phonon modes and angles of incidence.

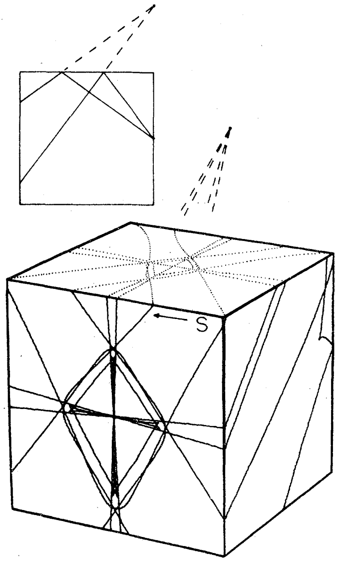

FIG. 13. Calculation of the specular reflection of singularity lines from top surface of the sample, as viewed in Fig. 12(a). The inset shows "real and virtual sources" (Ref. 14) and corresponding phonon paths as viewed along the [001] direction. The scan for determining the phonon reflection coefficient was taken along S.

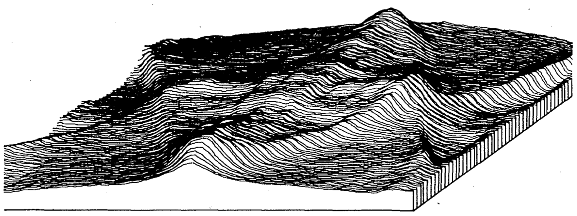

FIG. 14. Continuation of the time series in Fig. 9 to a later time, 8.95 μs. The new structure in the center is due to FTA ridge phonons reflected from the sides of the crystal which have a 14% greater path length than $l = 2.7$ cm.

The fact that the reflected phonon signal may be selectively enhanced by choosing a longer boxcar delay interval was especially apparent in the long Ge crystal. By continuing the time sequence of Fig. 9, we obtained the image traced in Fig. 14. At this longer delay time, a small square hump in the center of the pattern appeared, arising from FTA ridge phonons which were reflected from the side faces of the crystal.

V. THEORETICAL INTERPRETATION

In this section the mathematical developments in Sec. II and the Appendix are used to calculate and plot three-dimensional representations of the constant-frequency and group-velocity surfaces. From these two basic surfaces, the detailed origin of the phonon focusing patterns is exposed. The present discussion will be restricted to Ge, with known elastic constants $C_{11} : C_{12} : C_{44} :: 1.0 : 0.38 : 0.52$; however, we have performed similar calculations on other cubic crystals which indicate that phonons in Ge exhibit the principal topological behaviors found in other crystals. In fact, catastrophe theory limits the types of singularities possible. For this two-dimensional case only two types, fold and cusp, are possible.[36]

The constant-frequency $\vec{k}$-space surface for the STA mode in Ge is shown in Fig. 15(a). Plotted are lines of constant θ_k (latitude) and constant ϕ_k (longitude), restricted to the first octant of wave-vector space. The radial distance from the origin to the surface is $k = \omega / v(\theta_k, \phi_k)$. From this expression it is clear why the surface is called the "slowness surface."

The group-velocity surface, or wave surface, shown in Fig. 15(b) is constructed from Fig. 15(a) by transforming this $\vec{k}$-space grid of lines

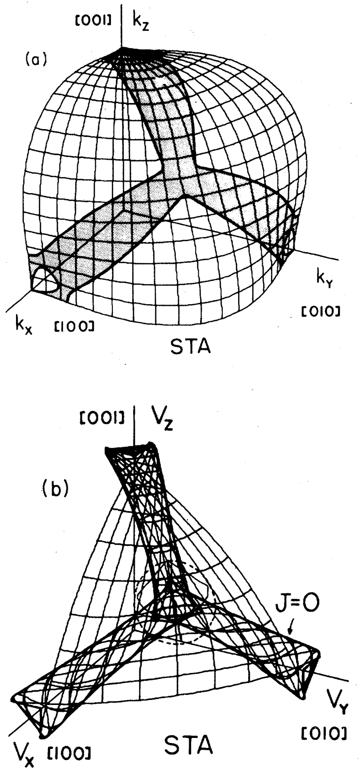

FIG. 15. (a) Slowness surface for the STA mode in Ge. The heavy lines are $J=0$ singularities, and the $J<0$ regions are shaded. (b) Group-velocity surface for STA mode in Ge.

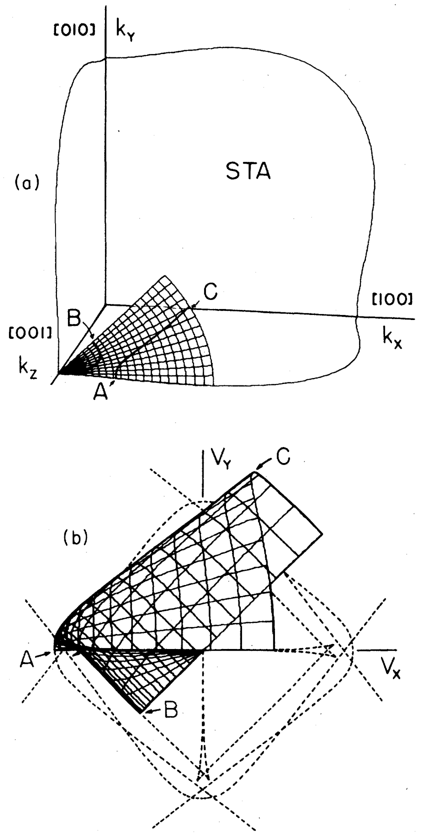

FIG. 16. (a) Symmetry-reduced segment of the STA slowness surface in Fig. 15(a) looking nearly along the z axis. (b) Section of the group-velocity surface from Fig. 15(b) corresponding to the $\vec{k}$-space segment in Fig. 16(a). Folds in this surface define the $J=0$ singularities in real space. The dashed lines show the position of singularity lines for the seven other symmetry-equivalent sections.

into their (θ_V, ϕ_V) directions at a radial distance $|\vec{V}|$. In general this surface may be folded, as in Fig. 15(b), such that along some directions there is more than one layer, or branch, to the surface. Each additional fold brings two additional branches along a given (θ_V, ϕ_V). Figure 15(b) provides a good rough overview of the focusing effect. A large grid density and number of branches on the group-velocity surface implies a large enhancement in that direction. If the constant-frequency surface has a well defined normal everywhere, then the group-velocity surface will be continuous and at any (θ_V, ϕ_V) the total number of branches will be odd. For transverse modes in Ge, however, there are symmetry directions, $\{111\}$, along which the normal to the constant-ω surface is undefined. The corresponding group-velocity surfaces have associated discontinuities. This phenomenon, known as conical refraction, will be discussed shortly.

The locus of points defined by $J(\theta_k, \phi_k)=0$ were found by a root-finding technique and plotted on the constant-frequency surface in Fig. 15(a). These lines separate regions of differing Gaussian curvature. The shaded region has negative Jacobian corresponding to a saddle-type curvature. This region separates the large convex areas centered about $\langle 110\rangle$ from the small concave areas near $\langle 100\rangle$, both of which have positive Jacobian. When transformed into $\vec{V}$ space these $J=0$ lines are found to fall on the folds of the group-velocity surface. An example of this in Fig. 15(b) is the ramp structure extending from the [001] to the [111] axis. To see the origin of this structure, follow a $\vec{k}$-space lattice line with $\theta_k \approx 40°$ from $\phi_k = 0°$ to 90°. The resulting ϕ_V increases monotonically to beyond 45°, but then reverses when the first $J=0$ line is crossed, forming a fold. As the $\vec{k}$ vector traverses the shaded region of Fig. 15(a), the group velocity undergoes a retrograde motion and ϕ_V decreases. When the second $J=0$ line is reached, ϕ_V again increases forming another fold. For angles in

$\vec{V}$ space between the folds there are three branches, or sheets, to the wave surface (see Fig. 18).

The enhancement of phonon flux $A = 1/|J|$, is mathematically infinite on a fold. As the phonon propagation direction (θ_V, ϕ_V) is scanned across a fold, the number of branches either increases or decreases by two, and there are different phonon flux enhancements on either side of the fold. Thus these singularity lines separate regions of high and low intensity as was observed in the ballistic phonon images. The asymmetry around these singularities can easily be seen in Fig. 8(b).

Figure 16 is a close-up of the STA surfaces as viewed along the [001] axis in Fig. 15. The grid covers $0 \leqslant \theta_k \leqslant 30°$ and $0 \leqslant \theta_k \leqslant 45°$. This range of ϕ_k is the minimum required for a complete symmetry-reduced description about the [001] axis. Figure 16(b) is the section of the group-velocity surface corresponding to this $\vec{k}$-space grid. The points marked A and B are in symmetry planes and do not transform out of those planes. The $J = 0$ line from A to C in Fig. 16(b) forms part of the outer square and ramps in Fig. 7(b). The singularity line from the [001] axis to point B likewise forms the inner square. As one follows the $J = 0$ singularity in $\vec{k}$ space from the [001] direction to point B the group velocity traces a cusped 45° vee pattern. The cusp corresponds to a point on the $J = 0$ line where the direction of zero principal curvature of the slowness surface lies *along* the $J = 0$ line. The cusped vee's are seen to comprise the inner square and diagonals observed in the experimental image. Other symmetry-equivalent $J = 0$ lines are shown as dashed lines in the figure. Due to the complex folding of the velocity surface near the [001], the STA mode has up to 11 branches. In contrast to this, the FTA mode has at most three, and the LA only one. The actual number or branches in each region for the STA mode is shown in Fig. 7(b).

The cusped-vee structure described near the [001] direction also occurs near the [111] direction in the STA mode. The calculated real-space $J = 0$ lines centered about the [111] are shown in Fig. 17(a). This pattern is the termination of three of the ramp structures emanating from the [100], [010], and [001] directions. Figure 17(b) is a section of the STA group-velocity surface for $\vec{k}$ vectors between three and seven degrees from the [111] axis in $\vec{k}$ space. In this case the $\vec{k}$-space grid is centered about the [111] axis and includes only lines extending radially from the [111]. This figure shows the complex topological structure of the cusp region. The cusp corresponds to the termination of two folds in the group-velocity surface.

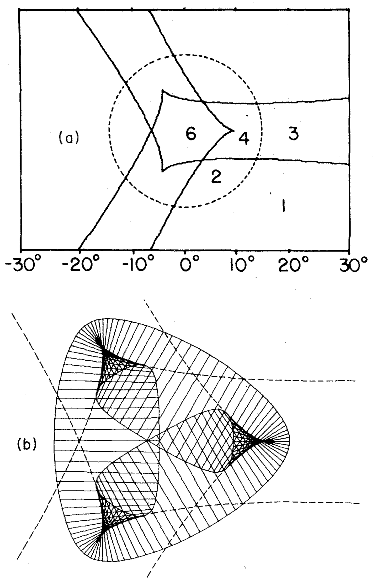

FIG. 17. (a) Real-space singularity lines for the STA mode projected onto the (111) plane. The [111] propagation direction is at the center. The scale at the bottom measures the propagation angle, in degrees, from the [111] axis. The integers are the number of STA branches. The FTA mode has one branch outside the dashed circle and none inside. (b) Section of the STA group-velocity surface for $\vec{k}$ vectors between 3° and 7° from the [111] axis, with the outer edge corresponding to $\vec{k}$ vectors 3° away from the [111]. The dashed lines show the continuation of the fold singularities which form the ramp structure in Fig. 15(b).

The sign of the Jacobian has another interesting geometrical interpretation, illustrated in Fig. 18. If one generates an infinitesimal clockwise circle on the slowness surface, the corresponding locus of $\vec{V}$ vectors will be clockwise

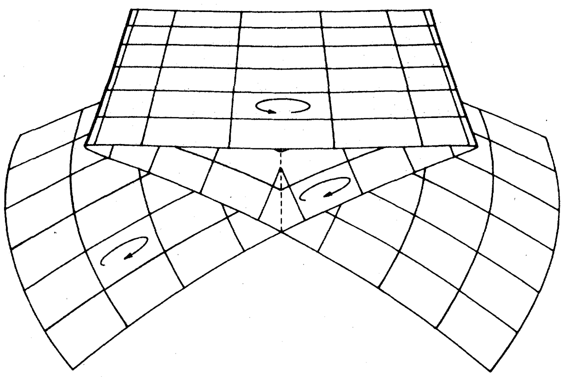

FIG. 18. Magnified section of the folded group-velocity surface (ramp structure) of Fig. 15(b). The sense of rotation on the surface is directly related to the sign of J as discussed in the text.

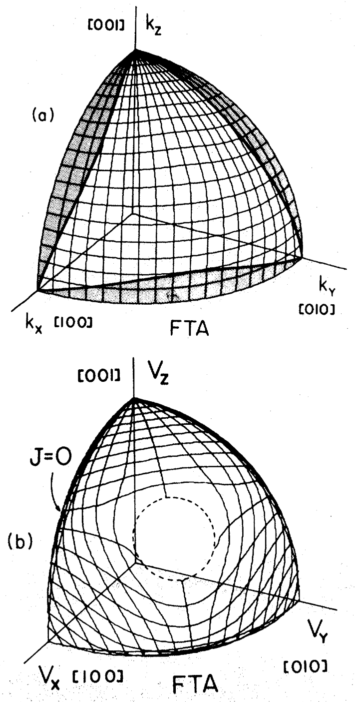

FIG. 19. (a) Slowness surface for the FTA mode in Ge. Shaded regions have ($J<0$) saddle curvature; all other regions have $J>0$. (b) Group-velocity surface for FTA mode in Ge. Note that this portion of the surface, corresponding to (a), extends slightly into other octants.

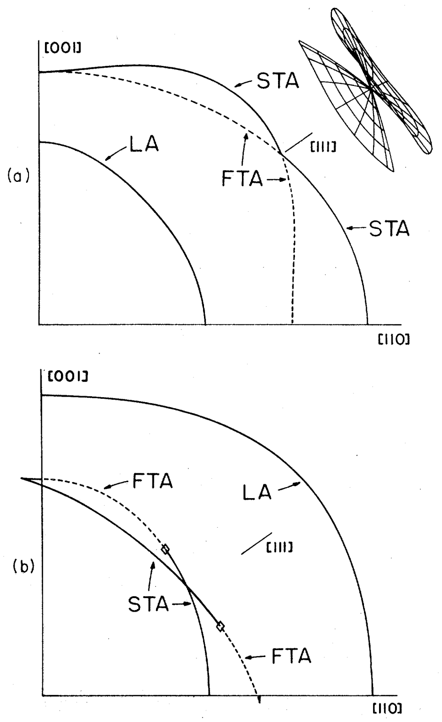

FIG. 20. (a) Intersection of the three Ge slowness surfaces with the (110) plane showing the conic contact between FTA (dashed line) and STA (solid line) at the [111] direction. Slightly out of this plane, the two transverse modes do not touch each other. The inset shows the three-dimensional nature of this contact. (b) Intersection of the group-velocity surfaces with the (110) plane. For the STA mode, only branches from the (110) plane in $\vec{k}$ space are shown. The small diamonds mark the continuous transition from STA to FTA and correspond to $\vec{k} \parallel [111]$ in Fig. 20(a).

when J is positive and counterclockwise when J is negative. A fold effectively inverts the group-velocity surface and this changes the above rotational sense. Generally when $J=0$ the $\vec{k}$-space circle transforms into a line.

The slowness and group-velocity surfaces for the FTA mode are shown in Fig. 19. The slowness surface is divided into regions of saddle curvature (shaded) and convex curvature (unshaded). The heavy lines are $J=0$ lines which separate the two regions. The corresponding group-velocity surface for the FTA mode is much less complex than that for the STA mode. The saddle regions near the {100} planes produce a folded group-velocity surface with structure analogous to the STA ramp structure. In this case the group-velocity surface extends into the adjoining V-space octant and then folds back to the {100} planes. The result is a narrow region between $J=0$ folds which produces the ridges in the ballistic phonon images.

In addition the FTA mode also has a large region about the [111] direction in which there are no branches at all. This area is outlined by the dashed curve in Fig. 19(b) and comprises a cone of half-angle 14.4°. This discontinuity in the group-velocity surface, which is complemented by another discontinuity in the STA mode along the same directions, is caused by conical refraction. This unusual behavior is precipitated by the fact that the FTA and STA constant-ω surfaces along the ⟨111⟩ directions have undefined normals. The two transverse modes have differing phase velocities in all directions except the ⟨100⟩ and the ⟨111⟩, where they are degenerate. Thus the FTA slowness surface lies entirely within the STA surface except for the ⟨100⟩ and ⟨111⟩ directions, where the surfaces touch. At the ⟨100⟩ these surfaces have a flat point of contact such that each has a well defined normal at that point. This is not true for the ⟨111⟩ directions, though. Here the surfaces have a pointed or conical contact.

The intersection of the LA, STA, and FTA constant-frequency surfaces with the (1$\bar{1}$0) plane is plotted in Fig. 20(a). A three-dimensional view showing the conical nature of the [111] contact between the FTA and STA is shown in the inset.

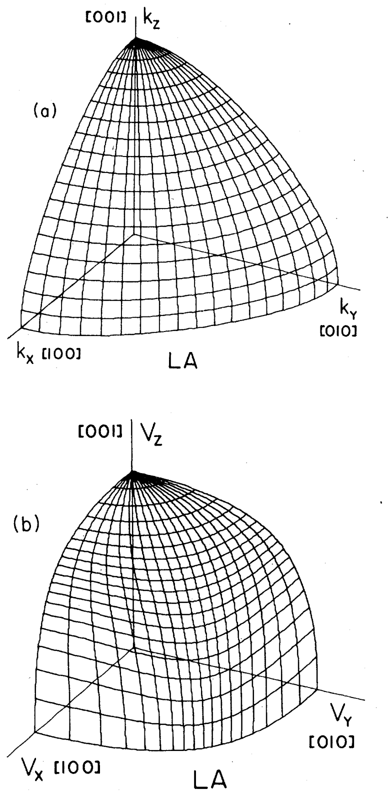

FIG. 21. (a) Slowness surface for LA mode in Ge. The surface is entirely convex. (b) Group-velocity surface for the LA mode in Ge, showing greatest grid density and hence greatest enhancement along the [111] direction.

The group velocities corresponding to Fig. 20(a) are shown in Fig. 20(b). The diamonds mark the intersection of the FTA and STA group-velocity surfaces, corresponding to $\vec{k} \parallel [111]$. In three dimensions this intersection forms the dashed circle in Figs. 15(b) and 19(b). Within this circle the STA mode has 2, 4, or 6 branches and the FTA has 0 branches, as shown in Fig. 17(a). Considered individually the FTA and STA group-velocity surfaces are discontinuous at this circular boundary, but, considered together they form a continuous surface. The conical refraction effect at $\vec{k} \parallel [111]$ produces no observable effect in flux enhancement in our ballistic phonon images for two reasons. First, no corresponding discontinuities in the phonon flux are predicted, and second, the large curvature in the slowness surface near [111] produces a defocusing of phonon energy.[37]

For completeness we show the slowness and group-velocity surfaces of the LA phonon mode in Fig. 21. While these phonons are noticeably enhanced near {111}, as indicated by the denser grid structure in Fig. 21(b), there are no singularities in the phonon flux. The group-velocity surface has no discontinuities and one branch everywhere. The enhancement factor ranges from $A = 0.21$ for $\vec{V} \parallel [100]$ and $A = 1.5$ for [110], to $A = 2.5$ for [111]. These numbers agree with the calculation by Maris.[8]

VI. CONCLUDING REMARKS

The present work offers a new geometric visualization of ballistic phonon propagation in crystals. The experimental imaging method provides an efficient and quantitative means for characterizing the anisotropic energy flux emanating from a point source of heat. The large angular variations in heat flux observed for Ge represent typical behavior for most crystals, cubic or not. Theoretically, the fold and cusp singularities studied here are a natural consequence of the two-dimensional transformation from $\vec{k}$ space to real space, involving the fourth-rank elasticity tensor. The mathematical origins of these singularities are readily traced to a vanishing of the total (Gaussian) curvature of the slowness surface which creates folds and cusps in the groups-velocity surface. These geometrizations of the phonon focusing in Ge give useful insights into the complex flux patterns which were discovered by the heat-pulse imaging method. By concentrating on the structure of the singularity patterns, a quantitative comparison with theory has been made which is quite independent of the exact detector shape.

Looking toward future applications, we expect that two-dimensional heat-pulse scanning will find use in the study of phonon scattering from interfaces, and possibly from defects, impurities, and free carriers. In cases where laser-scanning is not convenient, a knowledge of the anisotropic flux pattern in a given material is important for optimization of the generator-detector geometry. When scanning is possible, the imaging method converts the inherent anisotropies in phonon flux from a complex annoyance into a quantitative tool. As an example, the steps in phonon intensity produced by scanning across the fold in a group-velocity surface can be used to measure the absolute reflectivity of terahertz phonons from an interface. Attempts in the past to study phonon reflection using multiple detectors have met with difficulties due to sharp anisotropies in flux. Along another line, there is a growing interest in the propagation of short-wavelength acoustic phonons. It would be interesting and informative to observe changes in the structure of the phonon flux pattern for phonons produced high on the dispersion curve. The topology of the $\omega(\vec{k}) =$ constant surface should change radically for these high frequencies. Recent experiments on several materials[38,39] have demonstrated that very short-wavelength acoustic phonons created by thermal pulse or photoexcitation can travel macroscopic distances before down-converting. The ability accurately and continuously to time- and space-resolve phonons in a heat pulse opens a wide range of new experimental possibilities.

ACKNOWLEDGMENTS

We greatly appreciate the help and interest of A.C. Anderson, which made these experiments possible. Our ultrapure Ge samples were generously supplied by E.E. Haller and W.L. Hansen of Lawrence Berkeley Laboratory. M.A. Tamor and M. Greenstein made essential contributions to the computer-controlled imaging system. Both the experimental control and theoretical calculations were accomplished on this microprocessor-based system. The interfacing hardware and image-processing software were developed under the NSF Grant No. DMR-77-11672. This work was supported by the National Science Foundation under the Materials Research Laboratory Grant No. DMR-77-23999 and by a Cottrell equipment grant.

APPENDIX: PHASE-VELOCITY DERIVATIVES BY IMPLICIT DIFFERENTIATION

The phonon-focusing calculation requires a determination of the first and second derivatives of the phase velocity with respect to the wave normal $\vec{n} \equiv \vec{k}/|\vec{k}|$. In order to determine the derivatives $\partial v/\partial n_i$ and $\partial^2 v/\partial n_i \partial n_j$, we introduce a method employing implicit differentiation. The characteristic equation for the eigenvalue v^2 is

$$\det(D_{il} - v^2 \delta_{il}) = 0 \tag{A1}$$

with $D_{il} = (1/\rho)\, c_{ijlm}\, n_j n_m$. Defining $v^2 \equiv X$, this equation may be rewritten as

$$X^3 + QX^2 + RX + S = 0, \tag{A2}$$

where Q, R, and S are polynomials in the given c_{ijlm}'s and $\vec{n}$. The solutions for the three real roots are

$$X_\alpha = Y_\alpha - \tfrac{1}{3}Q \tag{A3}$$

where

$$Y_\alpha = 2\sqrt{a/3}\,\cos(\psi + \tfrac{2}{3}\pi\alpha), \quad \alpha = 0, 1, 2,$$

$$\psi = \tfrac{1}{3}\cos^{-1}[(-b/2)/(a^3/27)^{1/2}],$$

$$a = \tfrac{1}{3}Q^2 - R,$$

$$b = \tfrac{2}{27}Q^3 - \tfrac{1}{3}QR + S.$$

In principle, one can obtain the desired derivatives by brute-force differentiation of Eq. (A3), but considering that Q, R, and S are polynomials in the n_i, this is a very tedious method. In particular the cosine and inverse cosine functions produce trigonometric functions throughout the formulation via chain-rule differentiation, making it susceptible to numerical difficulties. An alternative is to differentiate Eq. (A2) implicitly. One finds

$$\frac{\partial X}{\partial n_i} = -\frac{\beta_i}{\gamma}, \tag{A4}$$

in which $\gamma = 3X^2 + 2QX + R$, and

$$\beta_i = \frac{\partial Q}{\partial n_i}X^2 + \frac{\partial R}{\partial n_i}X + \frac{\partial S}{\partial n_i}.$$

Also,

$$\frac{\partial^2 X}{\partial n_i \partial n_j} = -\frac{1}{\gamma}\left(\frac{\partial \beta_i}{\partial n_j} + \frac{\partial \gamma}{\partial n_j}\frac{\partial X}{\partial n_i}\right), \tag{A5}$$

in which

$$\frac{\partial \gamma}{\partial n_j} = (6X + 2Q)\frac{\partial X}{\partial n_j} + 2\frac{\partial Q}{\partial n_j}X + \frac{\partial R}{\partial n_j}$$

and

$$\frac{\partial \beta_i}{\partial n_j} = \left(2\frac{\partial Q}{\partial n_i}X + \frac{\partial R}{\partial n_i}\right)\frac{\partial X}{\partial n_j} + \frac{\partial^2 Q}{\partial n_i \partial n_j}X^2 + \frac{\partial^2 R}{\partial n_i \partial n_j}X + \frac{\partial^2 S}{\partial n_i \partial n_j}.$$

Given the differential relation $dX = 2v\,dv$, these equations give analytic expressions for the derivatives of the phase velocity required in Eq. (7). In component form,

$$V_i = \left(v - n_j\frac{\partial v}{\partial n_j}\right)n_i + \frac{\partial v}{\partial n_i}. \tag{A6}$$

The Jacobian in Eq. (10) further involves the derivatives of the group velocity:

$$\frac{\partial V_i}{\partial n_j} = \left(v - n_l\frac{\partial v}{\partial n_l}\right)\delta_{ij} + \frac{\partial^2 v}{\partial n_i \partial n_j} - n_i n_l\frac{\partial^2 v}{\partial n_l \partial n_j}, \tag{A7}$$

which makes use of $\partial^2 v/\partial n_i \partial n_j$ determined above. Specifically, the Jacobian may be calculated from the derivatives

$$\frac{\partial f}{\partial n_i} = \frac{1}{V}\left(\frac{\partial V_z}{\partial n_i} - \frac{V_z}{V}\frac{\partial V}{\partial n_i}\right),$$

$$\frac{\partial g}{\partial n_i} = \left(V_x\frac{\partial V_y}{\partial n_i} - V_y\frac{\partial V_x}{\partial n_i}\right)\Big/(V_x^2 + V_y^2), \tag{A8}$$

and the chain rules, $\partial f/\partial \cos\theta = (\partial f/\partial n_i)(\partial n_i/\partial \cos\theta)$, etc. This mathematical formulation is not specific to any particular crystal symmetry.

[1] O. Weis, Z. Angew. Phys. 26, 325 (1969).

[2] R. J. von Gutfeld and A. H. Nethercot, Phys. Rev. Lett. 12, 641 (1964).

[3] B. Taylor, H. J. Maris, and C. Elbaum, Phys. Rev. Lett. 23, 416 (1969).

[4] B. Taylor, H. J. Maris, and C. Elbaum, Phys. Rev. B 3, 1462 (1971).

[5] F. Rösch and O. Weis, Z. Phys. B 25, 101; 25, 115 (1976).

[6] A. K. McCurdy, in *Proceedings of the Third International Conference on Phonon Scattering in Condensed Matter*, edited by H. J. Maris (Plenum, New York, 1980), p. 341; J. Philip and K. V. Viswanathan, Phys. Rev. B 17, 4969 (1978).

[7] See, for example, C. Elbaum, in *Proceedings of the International Conference on Phonon Scattering in Solids, Paris*, edited by H. J. Albany (Comptes Rendus, Saclay, 1972), p. 1.

[8] H. J. Maris, J. Acoust. Soc. Am. 50, 812 (1971).

[9] J. C. Hensel and R. C. Dynes, in *Physics of Semiconductors, 1978*, The Institute of Physics Conference Proceedings No. 43, edited by B. L. H. Wilson (The Institute of Physics, London, 1978), p. 371.

[10] J. C. Hensel and R. C. Dynes, in *Proceedings of the Third International Conference on Phonon Scattering in Condensed Matter*, edited by H. J. Maris (Plenum, New York, 1980), p. 395.

[11] J. C. Hensel and R. C. Dynes, Phys. Rev. Lett. 43, 1033 (1979).

[12] G. A. Northrop and J. P. Wolfe, in *Proceedings of the Third International Conference on Phonon Scattering in Condensed Matter*, edited by H. J. Maris (Plenum, New York, 1980), p. 377.

[13] G. A. Northrop and J. P. Wolfe, Phys. Rev. Lett. 43, 1424 (1979).

[14] In fact the heat source is scanned and the detector is held fixed, as explained in Sec. III.

[15] In the past (e.g., Ref. 26) these folds have been called "cusps." We reserve the term cusp for a higher-order singular point on a fold.

[16] M. Lax and V. Narayanamurti, in *Proceedings of the Third International Conference on Phonon Scattering in Condensed Matter*, edited by H. J. Maris (Plenum, New York, 1980), p. 337.

[17] R. J. von Gutfeld and A. H. Nethercot, Jr., Phys. Rev. Lett. 17, 868 (1966).

[18] See, for example, *Proceedings of the International Conference on Phonon Scattering in Solids, Paris*, edited by H. J. Albany (Comptes Rendus, Saclay, 1972).

[19] See, for example, *The Helium Liquids*, edited by J. G. M. Armiatge and I. E. Farquar (Academic, New York, 1975), p. 473.

[20] See, for example, *Proceedings of the Second International Conference on Phonon Scattering in Solids*, edited by L. J. Challis, V. W. Rampton, and A. F. G. Wyatt (Plenum, New York, 1975).

[21] J. C. Hensel and R. C. Dynes, Phys. Rev. Lett. 39, 969 (1977).

[22] W. Eisenmenger, *in Proceedings of the Third International Conference on Phonon Scattering in Condensed Matter*, edited by H. J. Maris (Planum, New York, 1980), p. 303.

[23] P. Taborek and D. Goodstein, *in Proceedings of the Third International Conference on Phonon Scattering in Condensed Matter*, edited by H. J. Maris (Plenum, New York, 1980), pp. 215 and 219.

[24] P. Taborek and D. Goodstein, J. Phys. C 12, 4737 (1979).

[25] P. Taborek and D. Goodstein, Solid State Commun. 33, 1191 (1980).

[26] See, for example, M. J. P. Musgrave, Proc. R. Soc. London A 226, 339 (1954); G. F. Miller and M. J. P. Musgrave, *ibid.* 236, 352 (1956).

[27] M. J. P. Musgrave, *Crystal Acoustics* (Holden-Day, San Francisco, 1970).

[28] F. I. Federov, *Theory of Elastic Waves in Crystals* (Plenum, New York, 1968).

[29] E. B. Christoffel, Ann. Mat. Pura Appl. 8, 193 (1877); see also, A. G. Every, Phys. Rev. Lett. 42, 1065 (1979).

[30] R. J. von Gutfeld, *Physical Acoustics* (Academic, New York, 1968), Vol. 5, p. 223.

[31] Model *G*-300 PD optical scanners, General Scanning, Inc., 150 Coolidge Avenue, Watertown, MA 02172.

[32] Ge crystals ($N_D - N_A \leq 10^{12}$ cm^{-3} dislocation free) grown by E. E. Haller and W. L. Hansen of Lawrence Berkeley Laboratory.

[33] H. J. McSkimin and P. Andreatch, J. Appl. Phys. 34, 651 (1963).

[34] These data are similar to those published by Hensel and Dynes, Ref. 11, except that their bolometer was a 1-mm strip which integrated over one dimension. Also the theoretical plot of Fig. 8(b) corresponds to a point scan and was calculated by an analytic, not statistical, method.

[35] Indeed, Hensel and Dynes, Refs. 10 and 11, used an operational definition of fast and slow modes according to the relative group velocity. This usage however, leads to a confusion in the mathematical identity of a mode.

[36] P. Taborek (private communication). See T. Poston and I. N. Stewart, *Catastrophe Theory and its Applications* (Pitman, London, 1978).

[37] Hensel and Dynes, Refs. 10 and 11, ascribed peaks in phonon intensity near [111] to conical refraction. Actually, the peaks in their one-dimensional scan were due to the cusp and fold structure shown in Figs. 12(a) and 17, which arises from $\vec{k}$ vectors not along [111].

[38] D. Huet and J. P. Maneval, in *Proceedings of the Third International Conference on Phonon Scattering in Condensed Matter*, edited by H. J. Maris (Plenum, New York, 1980), p. 145.

[39] R. G. Ulbrich, V. Narayanamurti, and M. A. Chin, unpublished.

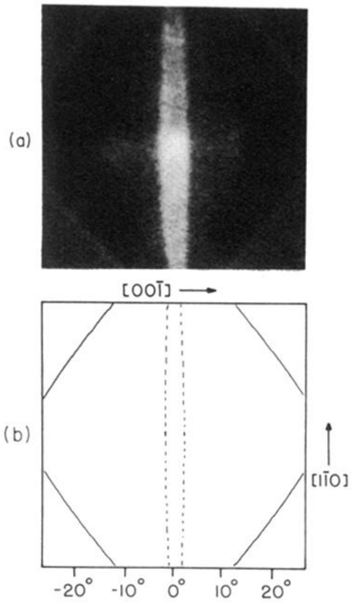

FIG. 10. (a) Phonon intensities obtained by scanning the heat pulse across a $(\bar{1}\bar{1}0)$ face and detecting with a bolometer at the center of the opposing (110) face. (b) Predicted $J = 0$ lines for the experimental geometry above. STA lines are solid and FTA lines are dashed. The scale at the bottom measures the propagation angle, in degrees, from the [110] axis.

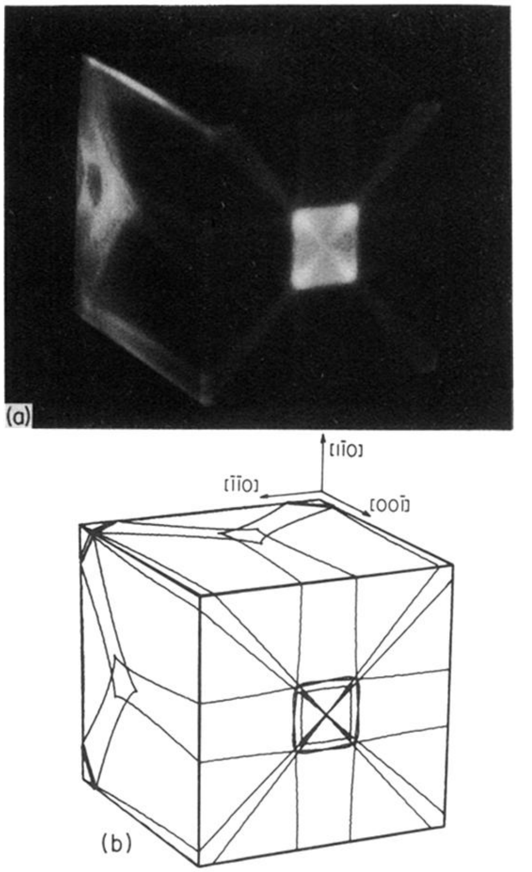

FIG. 11. (a) Ballistic phonon image with laser beam obliquely incident on three sample faces. The bolometer is in the center of the back left (001) face. (b) Calculated $J=0$ singularities projected onto an equivalent cube.

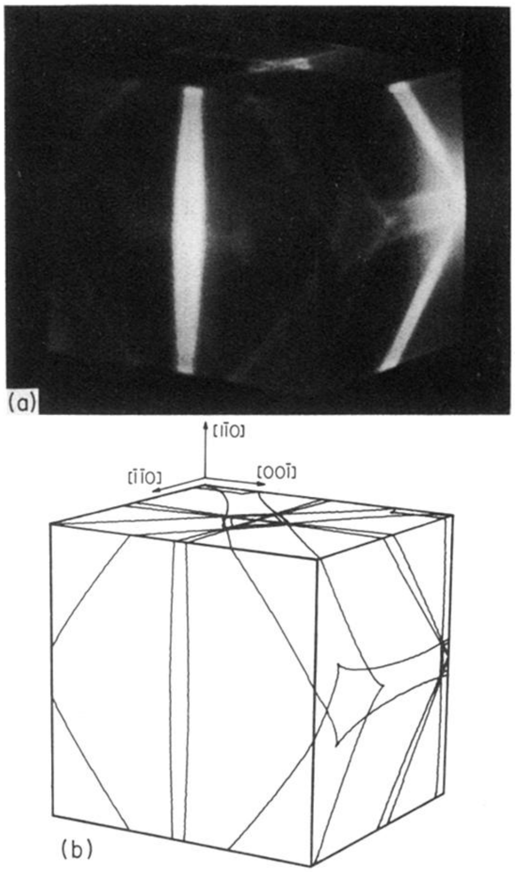

FIG. 12. (a) Same as 11(a) except slightly different orientation and with the bolometer in the center of the back right (110) face. (b) Calculated $J=0$ singularities projected onto an equivalent cube.

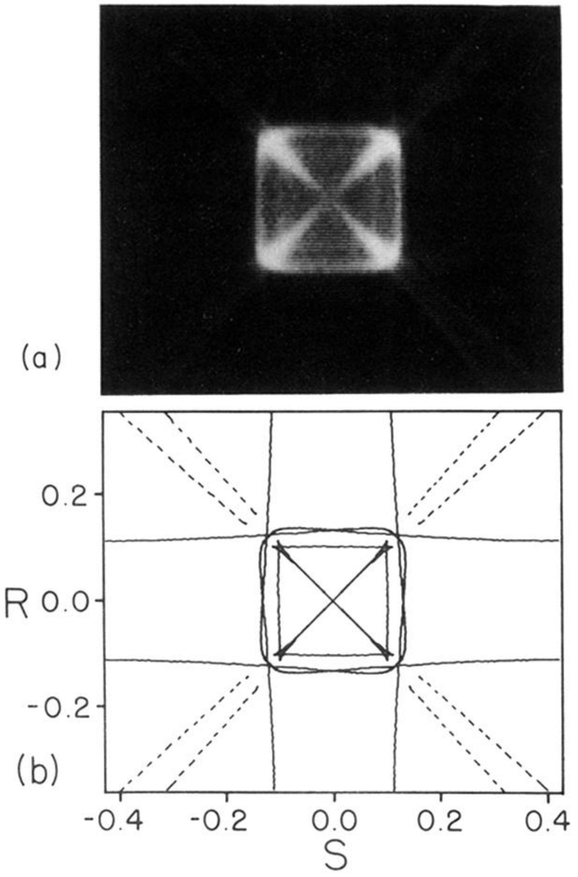

FIG. 2. (a) Ballistic phonon image for Ge. Bright regions indicate high phonon flux impinging on the (001) face of the crystal. This image represents a scan of 48° in propagation direction from left to right, with the [001] direction at the center of the pattern. The reader may find it useful to imagine a point source of phonons at the center of the pattern on the opposing face of the crystal (Ref. 14). (b) Calculated lines of mathematically infinite phonon flux for the xy scan in the image above. The solid lines are for the slow TA phonons and dashed lines are for fast TA phonons. The FTA singularity lines actually continue to the center. The axes are related to the propagation angles (θ_V, ϕ_V) by the relations $R = -\tan\theta_V \sin(\phi_V - \pi/4)$ and $S = \tan\theta_V \cos(\phi_V - \pi/4)$ obtained from Fig. 4(a).

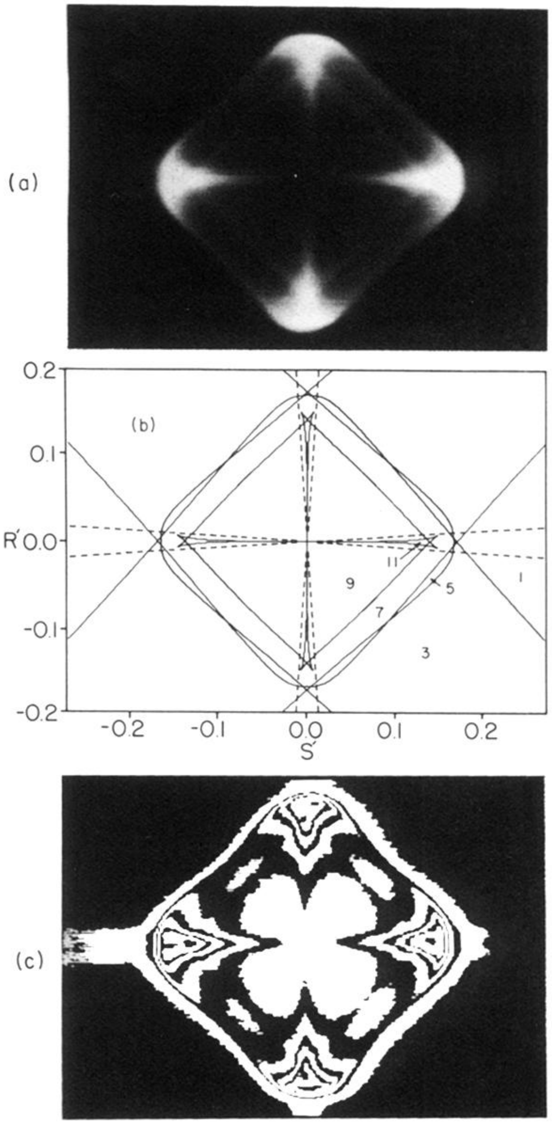

FIG. 7. (a) Magnified view of the TA phonon focusing structure near the [001] axis. The improved angular resolution and detail in the image results from the longer phonon path length in this crystal. The inner square and associated detailed structure is clearly visible in this photograph. (b) Calculated $J = 0$ lines for the same range of propagation directions as the above image. Solid lines are STA and dashed lines are FTA phonons. The integers indicate the number of branches of the group-velocity surface for the STA mode. The axes are related to the propagation angles (θ_V, ϕ_V) by the relations $R' = -\tan\theta_V \sin\phi_V$ and $S' = \tan\theta_V \cos\phi_V$ from Fig. 4(a). (c) Contour map of the ballistic phonon image in (a) defining curves of constant intensity.